

## VIABILITY

# A fast and effective method to assess myocardial necrosis by means of contrast magnetic resonance imaging

VINCENZO POSITANO, MS.C.,<sup>1,\*</sup> ALESSANDRO PINGITORE, M.D., PH.D.,<sup>1</sup> ASSUERO GIORGETTI, M.D.,<sup>1</sup> BRUNELLA FAVILLI, MS.C.,<sup>1</sup> MARIA FILOMENA SANTARELLI, PH.D.,<sup>1</sup> LUIGI LANDINI, PH.D.,<sup>2</sup> PAOLO MARZULLO, M.D.,<sup>1</sup> and MASSIMO LOMBARDI, M.D.<sup>1</sup>

<sup>1</sup>CNR Institute of Clinical Physiology, Pisa, Italy

<sup>2</sup>Department of Information Engineering, University of Pisa, Pisa, Italy

**Purpose.** Contrast magnetic resonance (CMR) can identify myocardial necrosis after gadolinium administration as a hyperenhanced (HE) area. Yet there are no software tools that can effectively quantify such an area. The aim of this study is to develop a robust and effective algorithmic method for defining the extent of myocardial necrosis evidenced through CMR. **Method.** Fifteen patients with previous myocardial infarction underwent nitrate Tetrofosmin G-SPECT and CMR. A software tool was developed, allowing semiautomatic detection of endocardial and epicardial borders and the automatic detection of HE regions. The accuracy of the proposed quantitative method of analysis has been tested with G-SPECT analysis that it is less than an ideal method for assessing myocardial viability, but at present is accepted and widely used in the clinical arena. **Results.** Segmental (SEHE) and global extension of HE were evaluated. HE was present in 161 of the 255 analyzed segments. Of the 161 HE segments, the mean SEHE was  $36 \pm 30\%$ . The operator independence (intraobserver:  $r = 0.97$ ,  $p < 0.0001$ , interobserver:  $r = 0.95$ ,  $p < 0.0001$ ) was good and significant, with noticeable time savings with respect to manual analysis. There was strong and inverse correlation between SEHE and scintigraphic regional uptake reduction ( $r = -0.66$ ,  $p < 0.0001$ ), and also a positive correlation between SEHE and SPECT defect extension ( $r = 0.75$ ,  $p < 0.0001$ ). When assessing the global extent of necrosis, the correlation between the two techniques was strong ( $r = 0.79$ ,  $p = 0.0004$ ). **Conclusions.** The proposed method of quantifying myocardial necrosis by CMR is highly reliable, reproducible, and operator-independent for quantifying.

**Key Words:** Myocardial necrosis; Contrast delayed enhanced MRI; G-SPECT; Automatic methods

## 1. Introduction

Myocardial viability is a fundamental issue in the clinical and therapeutical decision making process. The extent of viability correlates with recovery of contractile function after revascularization and thereby has relevant prognostic impact in patients with left ventricular dysfunction and coronary artery disease. Contrast magnetic resonance (CMR) can identify myocardial viability with different modalities using conventional morphological, perfusional, and functional parameters. Moreover, experimental and clinical studies show that CMR could directly visualize healed myocardium with delayed-contrast imaging (1, 2). Necrotic myocardium is identified as a hyper-enhanced (HE) area at the delayed acquired images after gadolinium administration. Moreover, the high spatial resolution of CMR and the high contrast between scar tissue and normal tissue elicit the assessment of the transmural extent of necrosis (3–5). Clinical studies show the accuracy of HE to identify the presence,

location, and transmural extent of myocardial necrosis (6, 7). When compared to positron emission tomography, HE had similar diagnostic accuracy for the detection of necrotic tissue, also identifying small subendocardial areas of necrosis not visualized by PET (8).

Despite the growing importance of CMR for evaluating myocardial necrosis, to date, no robust, effective, quantitative, operator-independent methods for assessing regional and global extent of HE are available. In this study, we present a complete software tool for assessing the global and segmental extent of myocardial necrosis, which provides numeric, bull's-eye, and 3D representations. In order to evaluate the effectiveness of this approach, the segmental and global extent of HE was compared with the distribution gated-SPECT (G-SPECT) perfusion abnormalities.

## 2. Material and methods

### 2.1. Patients

Fifteen patients (mean age  $63 \pm 6$  years) with previous (>3 months) myocardial infarction and resting perfusion defect at gated single-photon emission computed tomography

Received 5 June 2004; accepted 19 December 2004.

\*Address correspondence to Vincenzo Positano, Ms.C., CNR Institute of Clinical Physiology, Via Moruzzi, 1 56124, Pisa, Italy; Fax: +39-0503152166; E-mail: positano@ifc.cnr.it

(G-SPECT) and/or contractile abnormalities at echocardiography were consecutively enrolled in this study. The following was performed on all patients in random order and within 15 days: 1) 99 mTc-Tetrofosmin G-SPECT at rest following nitrate administration; 2) delayed-contrast magnetic resonance imaging for the assessment of delayed-contrast hyperenhancement. Informed consent was obtained for all patients. The protocol was approved from the institutional ethical committees.

## 2.2. Magnetic resonance imaging

Magnetic resonance imaging was performed using a 1.5 T whole body MR scanner (GE, CV/i, Milwaukee, WI) equipped with high performance gradient (40 mT/m amplitude, 150 mT/m/sec slew rate). A four-element (two anterior and two posterior) cardiac phased-array receiver surface coil was used for signal reception. A breath-hold segmented gradient echo fast imaging employing steady-state acquisition (FIESTA), electrocardiographic triggered sequence was used for the evaluation of regional and contractile function. The following parameters were used: echo time, 1.7 msec; repetition time, 4.0 msec; slice thickness, 8 mm with no interslice gap; field of view, 320 mm; data matrix size, 256 × 224 mm; phase of field, 0.75; trigger delay, minimum; views per segments, 8–14 according to the heart rate; flip angle, 45°. At least 30 cine frames were obtained for each slice. Post-contrast delayed images were acquired in the short axis of the left ventricle (LV) 20 minutes after bolus injection of 0.2 mmol/Kg of gadolinium-diethylenetriamine penta-acetic-acid (Gd-DTPA) in end-diastole for the evaluation of myocardial distribution of HE. A gradient echo based sequence with inversion prepulses (GRE-ET) was used with the following parameters: TE, 4.2 msec; flip angle, 20°; matrix, 256 × 160; NEX, 2.00; FOV, 36 cm; slice thickness, 8 mm. The inversion time ranged from 220 to 300 msec. A real-time option allowing the interactive change of inversion time was used to optimize this parameter until the nulling of myocardium was obtained. A variable number of short-axis slices (10 ± 1.8, maximum = 11, minimum = 8) were traced from the base to the apex to cover the entire left ventricle. Also, one vertical and one horizontal long-axis view were acquired to assess the apex.

## 2.3. Gated single photon emission computed tomography (G-SPECT)

Each patient underwent a resting G-SPECT following nitrate administration. Briefly, after the cannulation of an ante-cubital vein, the nitrate infusion started (isosorbide dinitrate 0.2 mg/mL, 10 cc/h). Criteria for radiotracer injection were: a drop in systolic blood pressure, ≥ 20 mmHg vs. rest systolic values, or an increase in heart rate, > 20 beats vs. rest heart rate. In the absence of evident hemodynamic effect, nitrate infusion was maintained for at least 20 minutes before radiotracer injection. Then 370–518 MBq of 99 mTc-Tetrofosmin

was administered, continuing the nitrate infusion for 5 minutes. Fifteen minutes later, patients had a fatty meal in order to accelerate tracer epatho-biliary clearance. About 45 minutes from radiotracer injection, a resting G-SPECT study was performed using a double head gamma camera (E.Cam, Siemens) equipped with high resolution collimators. A 64 × 64 matrix, 32 projections, 40 seconds/projection, eight frames/cycle protocol was employed together with a 15% window centered on the 140-keV photopeak of technetium-99m. The study was reconstructed using filtered back-projection without attenuation or scatter correction. A 12-lead electrocardiogram and blood pressure were monitored throughout the entire study. Postnitrate regional perfusion was assessed by means of quantitative perfusion score (QPS, E.Soft, Siemens). Such software allowed a completely automatic three-dimensional approach to quantify myocardial perfusion by G-SPECT, providing regional uptake reduction (RUR, % of maximal) of 99mTc-Tetrofosmin (9).

## 2.4. MR images analysis

CMR images in DICOM format were transferred to a dedicated workstation and processed by a dedicated software tool developed in IDL 6.0 environment. The developed software is available on request.

The method of analysis for the short axis images can be summarized as follows:

1. Semiautomatic evaluation of LV boundaries (i.e., endocardial and epicardial borders) along all acquired slices.
2. Automatic evaluation of HE area inside the LV boundaries (defined in the previous step) in each acquired slice.
3. Automatic placing of anatomical markers (i.e., the anterior and posterior septal insertion of the right ventricle) on one slice.
4. Automatic splitting of myocardium in number of radial sectors defined by the user, starting from the marker(s) defined in step 3. Sectors can be optionally divided into the inner and outer half (i.e., subendocardial and subepicardial layer).
5. Automatic evaluation of the extent of HE area defined in step 2 for each region defined in step 4.

The analysis of the two long-axis views proceeds instead as follows:

1. Manual definition of apex region in both images.
2. Automatic evaluation of HE area in the apex region previously defined.
3. Automatic evaluation of the extent of HE area defined in step 2 for the two apical regions.

After all images had been examined, the results were represented as bull's eye and 3D reconstruction.

Figure 1 shows the main phases of the methodology proposed for short-axis images: panel a shows original data.

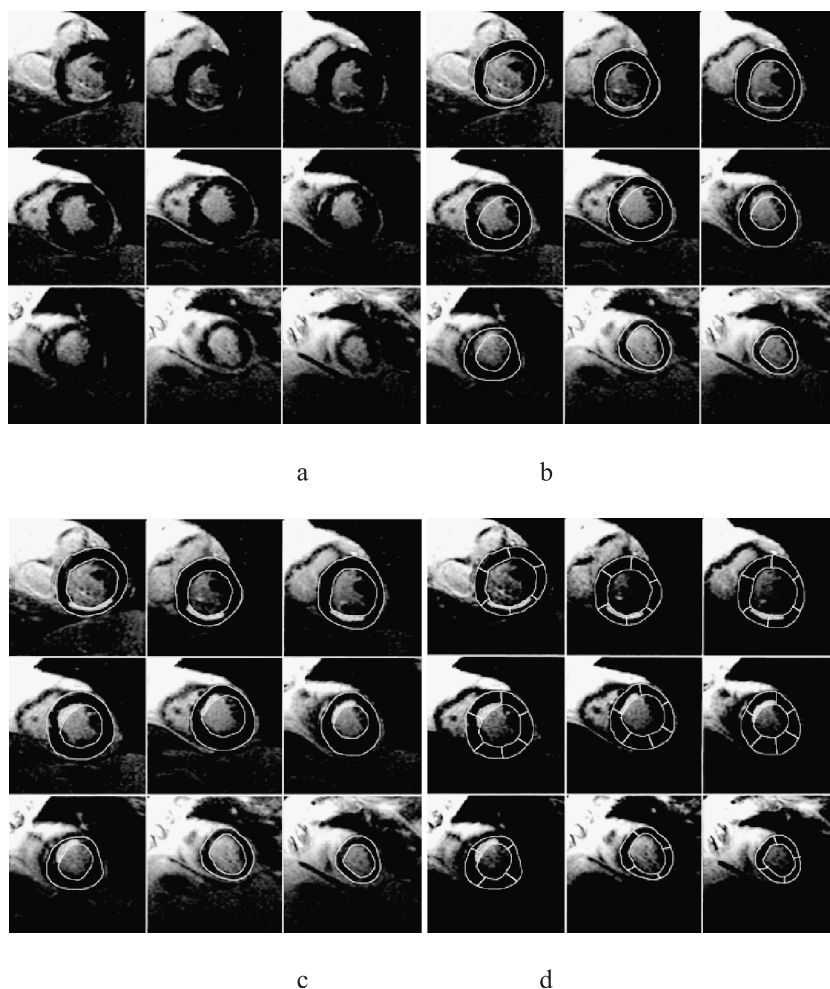


**Figure 1.** Method phases: original images (a), myocardial contour detection (b), hyperenhanced area detection (c), myocardium segmentation (d).

Panel b shows the semiautomatic definition of endocardial and epicardial border. Panel c shows the automatic definition of HE area. Panel d shows the automatic segmentation of myocardium.

### 2.5. Definition of LV boundaries

The inner and outer boundaries of the LV were defined on each short-axis image using an automatic method based on anisotropic filtering and active contour algorithm (10). A detailed theoretical description of the algorithm is provided in the appendix. In summary, the procedure starts from a rough, manually traced contour of internal LV cavity in one slice. From here, the inner and outer LV boundaries are automatically detected on all slices. The boundaries obtained are then examined by the operator and eventually corrected one by one.

### 2.6. Automatic definition of HE area

The HE regions in the myocardium were automatically extracted by fuzzy c-mean (FCM) clustering method that

automatically classified the myocardium in necrotic and normal regions. The FCM approach can perform unsupervised classification of data in a number of clusters, identifying different tissues in an image even without the use of an explicit threshold. The algorithm is detailed in the appendix. In our approach, the pixel values related to myocardial region were segmented into two clusters (i.e., HE and basal). The computer-generated results can then be corrected by the user.

### 2.7. Automatic definition of anatomical markers

The user must also define one or two reference points (i.e., the anterior and optionally posterior septal insertion of the right ventricle). The program attempts to define automatically those reference points that can be corrected by the operator.

### 2.8. Automatic splitting of myocardium

The myocardium can be automatically divided into a defined number of equiangular sectors starting from the reference point. In the present study, we used a 17-segment model of

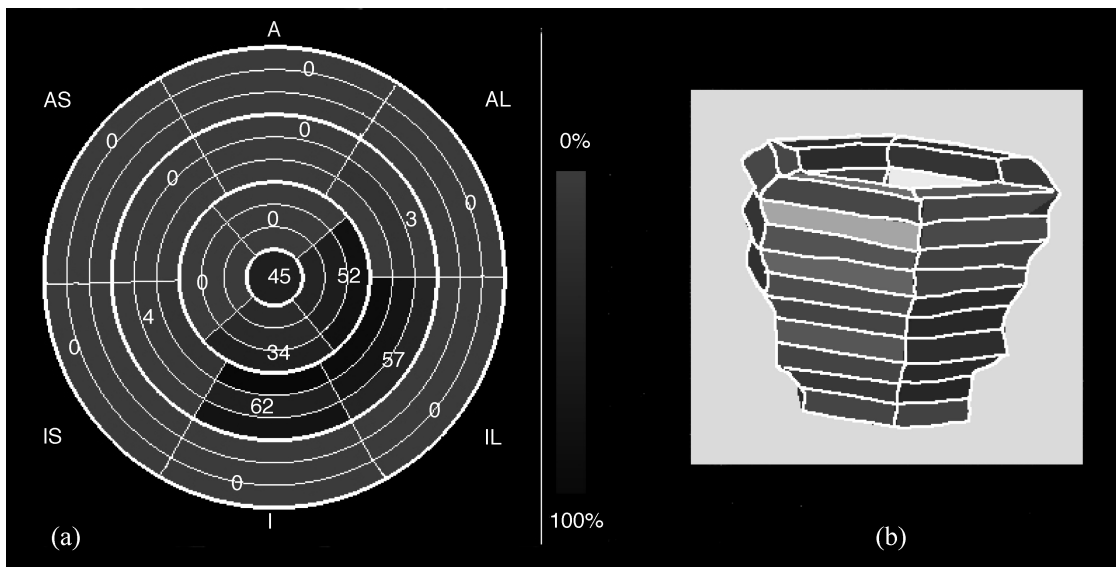


**Figure 2.** Bull's-eye (a) and 3D representation (b) of hyperenhanced area distribution. In the bull's-eye representation, the 17-sector model is highlighted.

the left ventricle, including six basal, six middle, four distal segments (inferior and anterior septum, anterior, antero-lateral, infero-lateral and inferior walls), and the apex (11).

### 2.9. Automatic evaluation of the segmental extent of HE

The myocardial mass related to each sector was evaluated, taking into account the geometrical information extracted from the DICOM files and a value of 1.05 g/mL for the density of the myocardial tissue. The method provided the values of the segmental myocardial mass and the segmental extent of HE (SEHE). SEHE was calculated as a percentage of HE with respect to the total segment area, according to the following formula:  $SEHE(\%) = (HEA \times 100) / (HEA + NEA)$ , where HEA is hyperenhanced area and NEA is unhyperenhanced area (12). The data from each sector were joined to obtain the values of necrotic mass of the left ventricle and its percentage with respect to the total myocardial mass. SEHE was divided into five clusters. The first cluster (less than 1% of SEHE) was identified as a sector with no HE. Clusters 2 to 5 correspond to SEHE values: cluster 2 = 1% to 25% of total area, cluster 3 = 26% to 50%, cluster 4 = 51% to 75%, cluster 5 = 76% to 100%.

## 3. Results

### 3.1. Visualization

Both numerical and bull's-eye representations of the 3D data volume were obtained. The values of SEHE were visualized by means of a bull's-eye, in which each value of SEHE is

represented in a color map. The more extended the HE, the darker was the corresponding segment (Fig. 2). The same data used in the bull's-eye were also represented as a 3D parametric map.

### 3.2. Post processing analysis

According to the 17-segmental model of the left ventricle, a total of 255 left ventricular regions have been examined for both CMR and SPECT techniques.

The mean processing time for each patient was  $5.25 \pm 1.5$  min. Table 1 shows the postprocessing time for the 15 subjects examined during the study with the number of slices acquired. In order to assess the robustness of the method, two operators, one blinded to the other, performed the analysis of the full data set. The intra-observer and inter-observer reproducibility was strong and significant ( $r = 0.97$ ,  $p < 0.0001$  and  $r = 0.95$ ,  $p < 0.0001$ , respectively).

In order to evaluate the advantages introduced by the semiautomatic procedure, data related to 10 subjects were processed by two operators on a GE-ADW workstation using a manual procedure consisting in drawing of ROIs. The mean manual processing time was  $26 \pm 3$  min. The inter-observer reproducibility was good but less than the one achieved by semiautomated analysis ( $r = 0.85$ ,  $p < 0.0001$ ). The agreement between manual and semiautomated analysis was good ( $r = 0.97$ ,  $p < 0.0001$ ).

### 3.3. Magnetic resonance vs. G-SPECT

The increase in signal intensity of HE areas was  $600\% \pm 75\%$ . HE was absent (cluster 0) in 94 (37%) of the

**Table 1.** Processing time in relation to the number of slices acquired and the extension of perfusion defect

Subject	Processing time	Number of slices	DE (SPECT)	HE (CMR)
#1	6 m 30 s	11	29	29
#2	5 m 30 s	9	39	33
#3	5 m 45 s	10	36	29
#4	5 m 00 s	10	19	11
#5	5 m 00 s	8	31	35
#6	5 m 30 s	11	7	9
#7	5 m 30 s	11	10	9
#8	5 m 45 s	11	26	24
#9	5 m 45 s	11	26	23
#10	4 m 30 s	8	38	25
#11	5 m 00 s	10	13	20
#12	5 m 30 s	9	35	27
#13	6 m 00 s	10	41	37
#14	5 m 0 s	10	14	11
#15	5 m 45 s	9	33	28

255 analyzed segments. Of the 161 hyperenhanced segments, the mean SEHE was  $36\% \pm 30\%$ ; SEHE was in cluster 1 in 67 segments (42%), in cluster 2 in 48 segments (25%), in cluster 3 in 25 (15%), and finally, in cluster 4 in 21 (13%). There was a strong and inverse correlation between SEHE and SPECT regional uptake reduction ( $r = -0.66$ ,  $p < 0.0001$ , 95% confidence interval for  $r = -0.72$  to  $-0.58$ ), and also a positive correlation between SEHE and SPECT defect extension ( $r = 0.75$ ,  $p < 0.0001$ , 95% confidence interval for  $r = 0.69$  to  $0.80$ ). When assessing the global extent of necrosis, the correlation between the two techniques was strong ( $r = 0.79$ ,  $p = 0.0004$ , 95% confidence interval for  $r = 0.46$  to  $0.92$ ). CMR had a tendency to underestimate the global extent of necrosis with a percentage of  $5.7 \pm 6.9\%$ .

#### 4. Discussion

Contrast-delayed enhancement can be considered a noninvasive method of CMR to directly evaluate the presence, site, and transmural extent of myocardial necrosis in human. In this study we adopted a quantitative method of analysis for assessing the global and segmental extent of HE. The proposed method allowed access to MR data in an effective way using the DICOM protocol and analyzing data in a software environment (i.e., IDL 6.0) commercially available.

This method allowed the automatic detection of epicardial and endocardial myocardial borders, automatic extraction of HE areas, and automatic and feasible segmentation of the zone of interest in a number of regions chosen by the user. Regional and global distributions of HE areas were provided as numerical values as well as bull's-eye and 3D graphical representations. This elicited the quantification of HE according to different spatial

coordinates: circumferentially, as the number of necrotic segments, and transmurally, as the extent of necrosis from the subendocardium to the subepicardium. Thus, patients with similar global extent of necrosis could be further divided according to the transmural extent of necrosis: into subjects with a predominantly transmural necrosis and subjects with predominantly subendocardial necrosis. The high robustness of this method was documented by the high inter-observer and intra-observer reproducibility. This depended particularly on the high signal intensity contrast between the normal and necrotic myocardium, which allowed good signal-to-noise ratio ( $8.2 \pm 1.7$ ) and contrast-to-noise ( $4.5 \pm 0.9$ ) ratio. We also adopted a real-time option for choosing the optimal inversion time to improve the signal intensity contrast between necrotic and normal myocardium. There was strong agreement between results obtained by the proposed methodology and manual analysis. Moreover, the time required for the analysis was reduced more than five times. This method also allowed the detection of small areas of myocardial infarction. In fact, two patients had small inferior infarction with a global extent of HE less than 7%; two segments were affected in one (basal and medium inferior wall) and one in the other (basal inferior wall). The segmental transmural extent was always less than 25% in these segments.

When compared to G-SPECT perfusion abnormalities, the global and segmental extent of HE matched closely the segmental and global extent of the percent regional radiotracer uptake. However, the discrepancies between the two methods may depend on the anatomical misalignment as well as the different spatial resolution of the two techniques, despite the fact that both CMR and G-SPECT are based on three-dimensional imaging and use the same planes for analysis. Also, the quantification of the extent of myocardial necrosis differs in the two methods: delayed enhancement quantifies myocardial necrosis as a continuous

variable, going from 0% to 100% of the segmental wall thickness, while G-SPECT defines the extent of myocardial necrosis by adopting threshold values. Moreover, G-SPECT has the tendency to overestimate the extension of necrosis, as compared to Thallium-201 or PET scan (13, 14), especially in those patients with severe left ventricular dysfunction, as in the present study. However, this limitation has been compensated for by using the quantitative analysis of regional radiotracer uptake (15, 16). The main limitation of the method proposed here was the detection of the myocardial borders. Many algorithms have been proposed to address the problem of the automatic segmentation of myocardium in MRI images, especially for the evaluation of LV function (17). However, the overall quality of CMR images is usually not good enough to allow detection of myocardial borders without user intervention. The proposed clustering technique in a fully automatic manner instead allows to detect HE areas effectively due to the high contrast between HE areas and the normal tissue.

The analysis of the apical region was based on a manual approach of the longitudinal slice; this could increase the inter- and intra-observer variability, thereby decreasing the method's accuracy in the evaluation of myocardial necrosis in this region. The application of the semiautomatic approach on the apical region should be realized to overcome this problem.

The accuracy of this quantitative method of analysis has been tested with G-SPECT which is less than an ideal method for assessing myocardial viability, but is well accepted and widely used for this purpose.

In conclusion, we developed a software tool that performs a semiautomatic and quantitative evaluation of contrast-delayed enhancement of CMR. Such a software tool shows good robustness and the results fit well with the results provided by G-SPECT. The availability of this method of analysis should increase the acceptance and utilization of contrast-delayed enhancement CMR in the routine clinical practice. Furthermore, the availability of quantitative measurements could make easier the comparison between different studies and patient follow-up.

## 5. Appendix

### 5.1. Anisotropic filtering and snake algorithm

The original snake algorithm (18) was improved using the adaptive anisotropic filter (19), which is able to:

1. Remove noise in regions of homogeneous physical properties (i.e., contrast medium), thus improving signal to noise ratio and contrast.
2. Enhance morphological definition by sharpening organ discontinuities.

The filtering method is described by the following equation

$$\frac{\partial}{\partial t} I(\mathbf{x}, t) = \text{div}[c(\mathbf{x}, t) \cdot \nabla I(\mathbf{x}, t)] \quad (1)$$

The diffusion strength is controlled by the conductance function  $c(\mathbf{x}, t)$ . The vector  $\mathbf{x}$  represents the spatial coordinate, while the variable  $t$  in our discrete implementation corresponds to iteration step  $n$ . The function  $I(\mathbf{x}, t)$  is the image intensity. Choosing a decreasing conductance function of the image gradient, the diffusion will be reduced or even blocked when close to an image discontinuity. The choice of the conductance function is critical for effectiveness of the algorithm and depends on the nature of the images. For CMR cardiac images we use (20):

$$c(\mathbf{x}, t) = \frac{1}{2} [\tanh(\gamma(k - \|\nabla I(\mathbf{x}, t)\|)) + 1] \quad (2)$$

The parameter  $\gamma$  controls the steepness of the min-max transition region, whereas  $k$  controls the extent of the diffusion region in terms of gradient gray-level.  $\gamma$  can be fixed to 0.2 for 256 gray-level images. In medical image processing, the  $\gamma$  value should be incremented proportionally to the range of the image values.

Starting from prefiltered images, a deformable model was developed as a curve that moves through the spatial domain of an image to minimize the following energy functional:

$$E = \int_0^1 \frac{1}{2} [\alpha |\mathbf{x}'(s)|^2 + \beta |\mathbf{x}''(s)|^2 + E_{\text{ext}}(\mathbf{x}(s))] ds \quad (3)$$

where  $\mathbf{x}(s) = [x(s), y(s)]$  and  $s \in [0, 1]$ ,  $\alpha$  and  $\beta$  control the mechanical properties of the snake, i.e., tension and rigidity respectively,  $\mathbf{x}'$  and  $\mathbf{x}''$  denote the first and the second derivatives of  $\mathbf{x}(s)$  with respect to  $s$ , and  $E_{\text{ext}}(\mathbf{x})$  is the potential associated to the external forces.  $E_{\text{ext}}(\mathbf{x})$  is derived from the image gradient so that it takes on its smaller values at the edge points. The external force can be defined to be a vector field  $\mathbf{v}(\mathbf{x})$  that minimizes the following functional:

$$\varepsilon = \int \int \mu |\nabla \mathbf{v}|^2 + |\nabla I|^2 |\mathbf{v} - \nabla I|^2 d\mathbf{x} \quad (4)$$

The external field  $\mathbf{v}(\mathbf{x})$  resulting from this calculation of variations is used in E expression as potential force  $-\nabla E_{\text{ext}}(\mathbf{x})$ , yielding:

$$\mathbf{x}_t(s, t) = \alpha \mathbf{x}''(s) - \beta \mathbf{x}''''(s) + \mathbf{v} \quad (5)$$

where  $\mathbf{x}''$  and  $\mathbf{x}''''$  are, respectively, the second and fourth derivative of  $\mathbf{x}(s)$  with respect to  $s$ . The GVF snake is represented by the parametric deformable surface solving the previous equation.

**5.2. Fuzzy C-mean cluster segmentation**

The fuzzy C-means (FCM) algorithm performs a classification of image data by computing a measure of membership, called the fuzzy membership, at each pixel for a specified number of classes. The fuzzy membership function, constrained to be between zero and one, reflects the degree of similarity between the image pixel at that location and the prototypical data value or centroid of its class. Thus, a membership value near unity means that the image pixel is close to the centroid for that particular class. FCM is formulated as the minimization of the following objective function with respect to the membership function  $u$  and centroids  $v$ :

$$J_{FCM} = \sum_{j \in \Omega} \sum_{k=1}^C u_{jk}^q \|y_j - v_k\|^2 \tag{6}$$

where  $\Omega$  represents the pixel location in image domain,  $q$  is a parameter greater than one that determines the amount of fuzziness of the classification ( $q = 2$  in our application),  $u_{jk}$  is the membership value at location  $j$  for class  $k$ ,  $y_j$  is the intensity value at  $j$  location,  $v_k$  is the centroid of the class  $k$ ,  $C$  is the number of classes ( $C = 2$  in our problem).

When the above objective function is minimized, the value of  $u_{jk}$  is approaching to one only if the pixel intensity at  $j$  location is close to the centroids of class  $k$ . Similarly, the value of  $u_{jk}$  is approaching zero only if the pixel intensity at  $j$  location is far from the centroids of class  $k$ . Also, the pixels with same intensity value would be grouped into the same groups with the same probability.

Minimization of  $J_{FCM}$  is based on the suitable selection of  $u$  and  $v$  using an interactive process through the following equations:

$$u_{jk} = \left( \sum_{i=1}^C \left( \frac{\|y_j - v_k\|^2}{\|y_j - v_i\|^2} \right)^{\frac{2}{q-1}} \right)^{-1} \tag{7}$$

$$v_k = \frac{\sum_{j \in \Omega} u_{jk}^q y_j}{\sum_{j \in \Omega} u_{jk}^q} \tag{8}$$

The algorithm stops when the value of  $u_{jk}$  converges.

**References**

1. Kim RJ, Fieno DS, Parrish TB, Harris K, Chen EL, Simonetti O, Bundy J, Finn JP, Klocke FJ, Judd RM. Relationship of MRI delayed contrast enhancement to irreversible injury, infarct age, and contractile function. *Circulation* 1999; 100:1992–2002.

2. Fieno DS, Kim RJ, Chen EL, Lomasney JW, Klocke FJ, Judd RM. Contrast enhanced magnetic resonance imaging of myocardium at risk: distinction between reversible and irreversible injury throughout infarct healing. *J Am Coll Cardiol* 2000; 36:1985–1991.
3. Klein C, Nekolla SG, Bengel FM, Momose M, Sammer A, Haas F, Schnackenburg B, Delius W, Mudra H, Wolfram D, Schwaiger M. Assessment of myocardial viability with contrast enhanced magnetic resonance imaging: comparison with positron emission tomography. *Circulation* 2002; 105:162–167.
4. Kim RJ, Wu E, Rafael A, Chen EL, Parker MA, Simonetti O, Klocke FJ, Bonow RO, Judd RM. The use of contrast enhanced magnetic resonance imaging to identify reversible myocardial dysfunction. *N Engl J Med* 2000; 343:1445–1453.
5. Wu E, Judd RM, Vargas JD, Klocke FJ, Bonow RO, Kim RJ. Visualization of presence, location, and transmural extent of healed Q-wave and non-Q-wave myocardial infarction. *Lancet* 2001; 357:21–28.
6. Ramani K, Judd RM, Holly TA, Parrish TB, Rigolin VH, Parker MA, Callahan C, Fitzgerald SW, Bonow RO, Klocke FJ. Contrast magnetic resonance imaging in the assessment of myocardial viability in patients with stable coronary artery disease and left ventricular dysfunction. *Circulation* 1998; 98:2687–2694.
7. Kitagawa K, Sakuma H, Hirano T, Okamoto S, Makino K, Takeda K. Acute myocardial infarction: myocardial viability assessment in patients early thereafter—comparison of contrast-enhanced MR imaging with resting 201Tl SPECT1. *Radiology* 2003; 226:138–144.
8. Kuhl HP, Beek AM, van der Weerd AP, Hofman MB, Visser CA, Lammertsma AA, Heussen N, Visser FC, van Rossum AC. Myocardial viability in chronic ischemic heart disease: comparison of contrast-enhanced magnetic resonance imaging with 18F-Fluorodeoxyglucose positron emission tomography. *J Am Coll Cardiol* 2003; 41:1341–1348.
9. Germano G, Erel J, Lewin H, Kavanagh PB, Berman DS. Automatic quantitation of regional myocardial wall motion and thickening from gated technetium-99 m sestamibi myocardial perfusion single-photon emission computed tomography. *J Am Coll Cardiol* 1997; 30(5):1360–1367.
10. Santarelli MF, Positano V, Michelassi C, Lombardi M, Landini L. Automated cardiac MR image segmentation: theory and measurement evaluation. *Med Eng Phys* 2003; 25:149–159.
11. Cerqueira MD, Weisman NJ, Dilsizian V, Jacobs AK, Kaul S, Laskey WK, Pennell DJ, Rumberger JA, Ryan T, Verani MS. Standardized myocardial segmentation and nomenclature for tomographic imaging of the heart: a Statement for Healthcare Professionals from the Cardiac Imaging Committee of the Council on Clinical Cardiology of the American Heart Association. *Circulation* 2002; 105(4):539–542.
12. Hillebrand HB, Kim RJ, Parker MA, Fieno DS, Judd RM. Early assessment of myocardial salvage by contrast-enhanced magnetic resonance imaging. *Circulation* 2000; 102:1678–1683.
13. Marzullo P, Sambuceti G, Parodi O. The role of Sestamibi scintigraphy in the radioisotopic assessment of myocardial viability. *J Nucl Med* 1992; 33:1925–1930.
14. Sawada SG, Allman KC, Muzik O, Beanlands RS, Wolfe ER Jr, Gross M, Fig L, Schwaiger M. Positron emission tomography detects evidence of viability in rest technetium-99 m-sestamibi defects. *J Am Coll Cardiol* 1994; 23:92–98.
15. Giorgetti A, Marzullo P, Sambuceti G, Di Quirico S, Kusch A, Landi P, Salvadori PA, Pisani P, Labbate A. Baseline/post-nitrate 99 mTc-Tetrofosmin mismatch for the assessment of myocardial viability in patients with severe left ventricular dysfunction: comparison with baseline 99 mTc-Tetrofosmin scintigraphy/18FDG-positron emission tomography imaging. *J Nucl Cardiol* 2004; 11(2): 142–151.

16. Dakik HA, Howell JF, Lawrie GM, Espada R, Weilbaecher DG, He ZX, Mahmarian JJ, Verani MS. Assessment of myocardial viability with  $^{99m}\text{Tc}$ -Sestamibi tomography before coronary artery by-pass graft surgery. Correlation with hystopatologic and postoperative improvement in cardiac function. *Circulation* 1997; 96:2982–2988.
17. Frangi AF, Niessen WJ, Viergever MA. Three-dimensional modeling for functional analysis of cardiac images, a review. *IEEE Trans Med Imag* 2001; 20:2–15.
18. Kass M, Witkin A, Terzopoulos D. Active contours models. *Int J Comput Vis* 1987; 1:321–331.
19. Perona P, Malik J. Scale-space and edge detection using anisotropic diffusion. *IEEE Trans Pattern Anal Mach Intell* 1990; 12(7):629–639.
20. Monteil J, Beghadadi A. A new interpretation and improvement of the non linear anisotropic diffusion for image enhancement. *IEEE Trans Pattern Anal Mach Intell* 1990; 12(7):940–946.